Shock Train Response to High Frequency Back Pressure Forcing

Alexander Gillespie* and Neil D. Sandham†

Aerodynamics and Flight Mechanics Group, University of Southampton, Southampton, UK, SO16 7PX

Numerical simulations are performed to study the effect of back pressure disturbances on a shock train. The basic problem consists of a shock train within a constant-area channel with a $M = 2$ inflow and a back pressure applied to the outlet. By subjecting the shock train to different fixed back pressures, it is shown that the shock train length varies linearly with back pressure, while the shock spacing is conserved. Through back pressure step forcing it is shown that the response of the shocks, after an initial lag, is largely determined by the magnitude of the step change. Step increases in back pressure cause upstream shock movements with higher shock pressures. The opposite response occurs with back pressure decreases. With sinusoidal back pressure forcing the shock train oscillates at the applied forcing frequency. The forcing propagates disturbances upstream and therefore there is a noticeable forcing-response lag. Higher frequency disturbances are filtered as they travel upstream through the shock train while lower frequencies induce larger shock oscillations and produce upstream offsets in the shock positions. Further examination of the flow reveals a region of low frequency motion below the leading shock which becomes strongly amplified by the lowest back pressure forcing frequency.

Nomenclature

(All variables are non-dimensional)

C	=	Sutherland constant
C_T	=	TENO cut-off parameter
E	=	Energy
f	=	Frequency
h	=	Channel half-height
l_x, l_y, l_z	=	Domain lengths
M	=	Mach number

---
*Present address: DSTL Portsdown West, Fareham, UK, PO17 6AD. E-mail address for correspondence: agillespie@dstl.gov.uk.
†Professor of Aerospace Engineering, Aerodynamics and Flight Mechanics Group. AIAA Senior Member.

N_x	=	Grid size
p	=	Pressure
p_b	=	Back pressure
Pr	=	Prandtl number
q	=	Heat flux
Re	=	Reynolds number
St_h	=	Strouhal number (based on half-height)
t	=	Time
T	=	Temperature
T_0	=	Period of oscillation
u	=	Velocity
x, y, z	=	Coordinates
γ	=	Specific heat ratio
δ_{99}	=	Boundary layer thickness
δ^*	=	Displacement thickness
$\Delta x^+, \Delta y^+, \Delta z^+$	=	Viscous grid spacing
θ	=	Momentum thickness
μ	=	Dynamic viscosity
ξ	=	Density scale factor
ρ	=	Density
τ	=	Viscous stress tensor

Subscripts

0	=	Condition at back pressure change
1	=	Condition at inlet
2	=	Condition at shock train leading edge
3	=	Condition at leading shock wave
4	=	Condition at second shock wave
i, j, k	=	Indices
lag	=	Condition after back pressure lag
r	=	Dimensional reference value
w	=	Condition at wall
vd	=	Relating to the van Driest profile

I. Introduction

S HOCK TRAINS are systems of linked shock wave/boundary layer interactions (SBLIs) which commonly occur in supersonic ducted flows [1]. From classical gas dynamics, a normal shock is created when a strong back pressure is applied to supersonic channel flow. However, given sufficient confinement ratio (boundary layer thickness divided by duct half-height: δ_{99}/h) and a sufficiently high Mach number (typically $M > 1.5$), the subsonic flow downstream of the shock is reaccelerated and an additional shock forms further downstream in order to satisfy the imposed pressure conditions. One particular type of shock train involves a series of normal or oblique shock waves in constant area ducts where the shocks form in response to an imposed back pressure [2–4]. This type of flow is typical of the isolator section of scramjet engines where the flow is compressed ahead of the combustor.

Within the shock train there are distinct supersonic and subsonic layers. The supersonic layer is characterized by repeated accelerations and decelerations through shocks and expansions, while the subsonic layer is a highly turbulent region of flow with considerable mixing and viscous interaction. This difference is most stark when comparing the pressure measurements at the centerline, where the pressure change is highly oscillatory, and at the wall, where there is a gradual pressure rise. Typically, at the end of the shock train the subsonic layer reaches the duct centerline such that the entire cross section of the channel becomes subsonic.

The main governing parameters affecting the behavior and structure of shock trains are generally considered to be the upstream Mach number (M_1), the confinement ratio (δ_{99}/h), and the exit/inlet pressure ratio (p_b/p_1). The Mach number strongly affects the SBLI structure and higher Mach numbers ($M_1 > 2$) are more commonly associated with the dominance of oblique shocks over normal shocks [5, 6]. Additionally, higher Mach number shock trains often exhibit more unsteady behavior, where the system has as a tendency to drift upstream towards the inlet [5]. In general, higher Mach numbers produce longer shock trains with wider spacing between the shocks due to the shallower Mach and shock angles [3, 7].

The confinement ratio quantifies the effect of the boundary layer and has a noticeable influence on the length of the shock train as well as the distance between shocks. With the use of schlieren photographs Carroll & Dutton [5, 8] were able to show that the overall length of the interaction scaled with the confinement ratio, with more boundary-layer dominated flows exhibiting a higher number of weaker shocks. A more recent study by Fiévet et al. [2], performed using direct numerical simulations on a similar layout at $M = 2$, confirmed these findings while also demonstrating the upstream displacement of the entire shock structure at increased levels of confinement.

When considering the shock train to be a physical response to a prescribed pressure condition, it is intuitive that a larger ratio between exit and inlet pressure should produce a more significant shock train response. The shock train length varies positively with back pressure, assuming that other variables can be kept constant, and the streamwise distribution of pressure at the wall is largely independent of the actual back pressure imposed, provided that the distribution is normalized by the location of the initial pressure rise [9].

Although Reynolds number (generally taken as Re_θ ahead of the shock train) also affects the structure of the shock train, the influence is known to be very weak. It is estimated that in circular and rectangular ducts, the shock train length only scales with $Re^{1/4}$ [1, 10] meaning that with an order of magnitude increase in Reynolds number one would only expect the shock train length to increase (relative to the duct height) by around 80%. By exploiting this weak scaling, researchers have been able to successfully reproduce wind tunnel experiments with numerical simulations at much lower (and therefore computationally affordable) Reynolds numbers [4, 11].

The bulk of shock train research is concerned with their static behavior i.e. studying instantaneous or time-averaged flow fields. However, due to the real world applications of shock trains (for example, in an isolator between a compression inlet and a combustor), the flow cannot be considered to merely exist in a steady state and so understanding time-dependent effects is important. A time-dependent back pressure can be used to study the impact of downstream combustion cycles on an isolator shock train. Applying a sinusoidal pressure function at the exit (by means of a numerical boundary condition or a hydraulic device) will cause the shock train to oscillate at the applied frequency in the streamwise direction. The oscillation pattern is that of an imperfect sinusoid, with an observed bias towards upstream movement both in terms of the response speed and the oscillation amplitude, with lower frequencies producing larger oscillation amplitudes [12]. Additionally, there appears to be an asymmetry of the shock position between upstream and downstream motion [13].

Most of the current research on back pressure forcing is concerned with a fairly narrow band of low frequencies - between 0.5 and 20Hz corresponding to Strouhal numbers based on duct half width (St_h) of the order 10^{-5} to 10^{-3}. At this frequency range the shock train moves as a quasi-rigid body since the time delay between the head and tail of the shock train is negligible [14]. A study by Jiao at al. [15] has considered the effects higher frequency forcing in the range 50-1000Hz ($St_h \sim 10^{-3}$-10^{-2}) where this time delay becomes non-negligible. Here the highest shock oscillation amplitude was found at 200Hz and the smallest at 1000Hz. It was noted that the peak oscillation occurring at an intermediate frequency suggested the presence of an excitation effect within the shock train.

In addition to back pressure forcing, there has also been a consideration of inflow perturbations by Fiévet et al. [2]. As part of this study, the inflow boundary layer thickness was varied over time as a sinusoidal function at a range of frequencies between 20 and 1000Hz. The variations in inflow pressure caused an oscillation in the shock train position. At particularly high frequencies the shock train acted as a low-pass filter and the size of the oscillations was small. Lower frequencies were generally responsible for larger oscillations although the peak occurred at around 93Hz due to an observed resonance-like effect (similar to that seen in [15]).

A common focus of research on incident-reflected SBLI flows is the analysis of the frequency space and the unsteady behavior of the shock structure. Spatial distributions of wall pressure power spectral density (PSD) provide useful insights into the unsteady behavior. It is well understood that a typical SBLI system is responsible for a broadband increase in fluctuation intensity. Additionally, there is a significant peak in low frequency motion corresponding to

location of the shock foot - this is observed both in simulations [16] and wind tunnel experiments [17]. This unsteadiness occurs at a frequency of the order $0.01u_1/\delta_{99}$ which is several orders of magnitude below the characteristic frequency of the inflow boundary layer. It was shown in [18] that the low frequency motion arises locally in the vicinity of the shock-induced separation, where the coupled shock-boundary-layer system acts as a low pass filter, requiring only the presence of broadband noise, whether from upstream or downstream. Similar frequency analysis has also been performed on shock trains, although the extent of the research is much more limited. Roussel [11] performed a spectral analysis of a Mach 1.6 shock train finding a peak of low frequency motion at the leading shock wave similar to that of canonical SBLIs (at a Strouhal number of around $St_L = 0.03$). This has also been observed by Xiong et al. [19] where the observed frequency was independent of a number of flow conditions (back pressure, duct geometry). These results suggest that the same physical mechanism of low frequency unsteadiness occurs in both oblique SBLIs and shock trains. Of particular interest in the present contribution is the response to downstream forcing, superimposed on the broadband disturbances already present in the turbulent boundary layer.

This work is focused on the shock train back pressure effects and particularly on high frequency sinusoidal forcing. A full account of the numerical arrangement, as well as validation of the grid and scheme sensitivity, us given in section II. In section III we consider the effect of fixed back pressures as well as the shock response to step forcing. Finally, simulation results of sinusoidal back pressure forcing and a discussion of the frequency effects are given in section IV.

II. Numerical Methodology and Validation

A. Methodology

All of the simulations in the current work are solved using a direct implementation of the compressible, dimensionless Navier-Stokes equations which are described in tensor notation by

$$\frac{\partial \rho}{\partial t} + \frac{\partial \rho u_j}{\partial x_j} = 0, \tag{1}$$

$$\frac{\partial \rho u_i}{\partial t} + \frac{\partial (\rho u_i u_j + p\delta_{ij})}{\partial x_j} - \frac{\partial \tau_{ij}}{\partial x_j} = 0, \tag{2}$$

$$\frac{\partial \rho E}{\partial t} + \frac{\partial (\rho E + p)u_j}{\partial x_j} - \frac{\partial q_j}{\partial x_j} - \frac{\partial \tau_{ij}u_i}{\partial x_j} = 0, \tag{3}$$

where ρ, T and E are respectively density, temperature and energy, and u_i are the velocity components. The pressure (p), the viscous stress tensor (τ_{ij}) and heat flux (q_i) are given by

$$p = (\gamma - 1)(\rho E - \frac{1}{2}\rho u_j u_j), \tag{4}$$

5

$$\tau_{ij} = \frac{\mu}{Re} \left(\frac{\partial u_i}{\partial x_j} + \frac{\partial u_j}{\partial x_i} - \frac{2}{3} \delta_{ij} \frac{\partial u_k}{\partial x_k} \right), \tag{5}$$

$$q_j = \frac{\partial T}{\partial x_j} \left(\frac{\mu}{(\gamma - 1) M^2 Pr Re} \right), \tag{6}$$

where Re is the Reynolds number, Pr is the Prandtl number, M is the freestream Mach number, γ is the heat capacity ratio and μ is the viscosity, defined by Sutherland's law

$$\mu = T^{3/2} \frac{1 + C}{T + C}, \tag{7}$$

with C denoting the Sutherland constant, obtained by

$$C = \frac{T_s}{T_r}. \tag{8}$$

Here T_s is the Sutherland temperature (110.4K) and T_r is the reference temperature (288.0K). Finally, pressure, density and temperature are related by the dimensionless ideal gas law:

$$p = \frac{\rho T}{\gamma M^2}. \tag{9}$$

In the current implementation, velocity, density, temperature and viscosity are non-dimensionalized by the freestream quantities (u_r, ρ_r, T_r), with pressure non-dimensionalized by $\rho_r u_r^2$. All distances are non-dimensionalized by the displacement thickness of the van Driest-transformed inflow profile, δ_{vd}^*. All of the simulations model air with $\gamma = 1.4$ and $Pr = 0.72$.

The governing equations are solved using OpenSBLI, an explicit, finite difference solver used for compressible turbulence problems [20, 21]. Shock capturing is applied to the Euler terms of the simulations with a 6-th order TENO scheme [22]. This scheme has good stability for shock wave problems and performs well with turbulence problems - for example, Lusher and Sandham [23] found very good agreement between the 6-th order TENO and 4-th order central schemes when simulating the Taylor-Green vortex problem.

The finite difference stencil reconstruction of the TENO scheme is composed a locally-determined combination of symmetrical and asymmetrical candidate stencils. Stencils which have to bridge across large discontinuities are not included in the final sum and thus the impact of spurious oscillations is minimized. The cut-off parameter (C_T) of the scheme determines the threshold for which stencils are included in the final combination. A lower C_T value means that larger flow discontinuities will be tolerated and thus the scheme will be less numerically stable, with the corollary being that the artificial dissipation of the problem will be lower. For static shock problems we use the recommended value of

$C_T = 10^{-6}$ while for moving shock problems a more stable value of $C_T = 10^{-5}$ is used. The effect of this parameter on a shock train configuration is given in section II.C. A 4-th order central scheme is used for the heat flux and stress terms and the time advancement is performed with a low-storage RK3 scheme [24].

An outline of the general flow configuration can be seen in fig 1. The arrangement consists of a long channel bounded above and below by solid surfaces and open at either side. Flow at $M_1 = 2$ enters from the inlet with turbulent boundary layers forming on the top and bottom walls. A back pressure is applied via a sponge zone at the exit such that a prescribed pressure ratio (p_b/p_1) is met and thus a shock train forms within the domain. The case dimensions in the standard Cartesian frame are $(l_x, l_y, l_z) = (16h, 2h, 1h)$, where h is the channel half-height. A streamwise distance of $6h$ downstream of the inflow is required for the turbulent boundary layer to develop, while the sponge zone occupies $2h$ from the outlet plane. The boundary layer properties at the inlet are $\delta_{99}/h = 0.28$ and $Re_\theta = 500$. Full details of the flow parameters at the inlet and just upstream of the shock train are given in table 1.
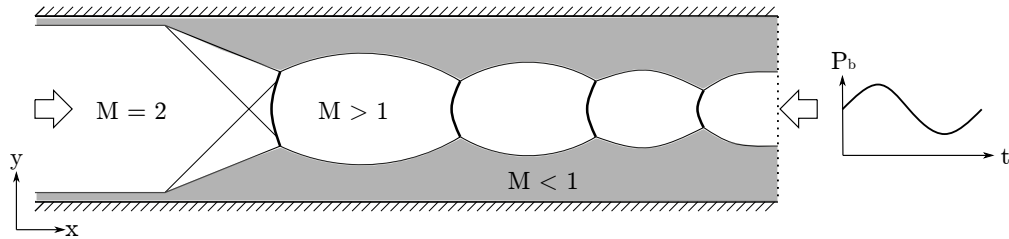

Fig. 1   Outline of the general flow arrangement.

Table 1   Summary of flow parameters at the inlet and shock train leading edge.

Location	δ_{99}/h	δ^*/h	θ/h	Re_θ	Re_θ	M_e
Inlet (1)	0.28	0.083	0.024	500	130	2.0
Shock train leading edge (2)	0.38	0.117	0.038	740	170	1.95

The boundary conditions on the top and bottom surfaces are applied as no-slip isothermal walls, with wall temperature $T_w/T_1 = 1.676$. Periodic conditions are applied in the z direction which mimics an infinite-span arrangement (note that resolving sidewalls can still have a significant effect on the structure of the shock train [4, 25, 26]). The boundary layer turbulence is generated using a synthetic turbulence generation method at the inflow plane. The particular method is a modified version of the one developed by Kim et al. [27, 28] where pseudo turbulent structures are randomly generated which are then carried downstream where they develop into physical turbulent structures. The development of these structures (what we will refer to as the boundary layer development region) occurs between $x = 0$ and $x = 6h$. After this point, the key boundary layer properties (skin friction, turbulence intensity, correlation lengths) are converged [25]. The spanwise integral length scales are of the order $0.1h$ meaning that the domain is sufficiently wide to avoid any synthetic windowing effects. Within the sponge zone a body-force term is applied to gently force the flow within the region to the

target back pressure condition, p_b. Additional information and validations of the sponge zone and turbulence generation can be found in chapters 3 and 4 of [25].

The Reynolds number of the current simulations is deliberately low in order to reduce the computational cost of running DNS cases. At the domain inflow the conditions are $Re_\theta = 500$ and $Re_\tau = 130$ which rise to 740 and 170 just upstream of the shock train. These values are significantly lower than published LES and DNS results, which are themselves typically much lower than comparable wind tunnel results. For example, the minimum Re_θ values reported in Morgan [4] and Fiévet [2] are respectively 1660 and 4350 (but with the viscosity multiplied by a factor of four to make the simulation more tractable). In general, the Reynolds number is found to have a very weak effect on the structure of the shock train - indeed the same configuration to the current work was tested with the Reynolds number up to a factor of two higher, finding only a limited impact on the shock train length and relative positions [25].

Typical flow fields of Mach number and density gradient are shown in fig 2. Here, a pressure ratio of $p_b/p_1 = 3.0$ is applied and a shock train comprising 4 shocks forms within the domain. Within the shock train there is a significant thickening of the boundary layer and a large portion of the flow cross-section becomes subsonic, although a marginally supersonic core remains in the sponge zone. The first shock, composed of two oblique shocks and a primary normal shock, causes a separation bubble (approximately $2h$ long) to form, as shown by the solid white lines in the Mach number plot. Further downstream there are additional pockets of transient separation inside the subsonic region. The remaining shocks in the shock train are approximately normal shocks. At each shock there is a small subsonic region after which the flow is reaccelerated.

B. Grid Refinement Study

A grid refinement study was carried out in order to understand the sensitivity of the shock train flow properties. Here we compare two grid resolutions (Baseline and Fine), with details listed in table 2. The Fine grid has a 50% higher resolution in each direction and (when adjusting for reduced timestep size) has a five-fold increase in computational cost over the Baseline grid. The reported viscous grid spacings correspond to upstream boundary layer conditions and, were it not for the presence of shock capturing, both grids would be considered as satisfying the usual conditions for direct numerical simulation. Both grid cases are run at the stated flow conditions in the previous section. A back pressure of $p_b/p_1 = 3.0$ is applied to each case.

Table 2 **Summary of grid resolutions upstream of the shock train** ($x = 6h$).

Grid	N_x	N_y	N_z	Δx^+	Δy^+ (min/max)	Δz^+
Baseline	800	320	60	9	0.8/5	8
Fine	1200	480	90	6	0.5/3.5	5

Results of the grid study are given in fig 3 where we compare the streamwise distributions of time- and span-averaged
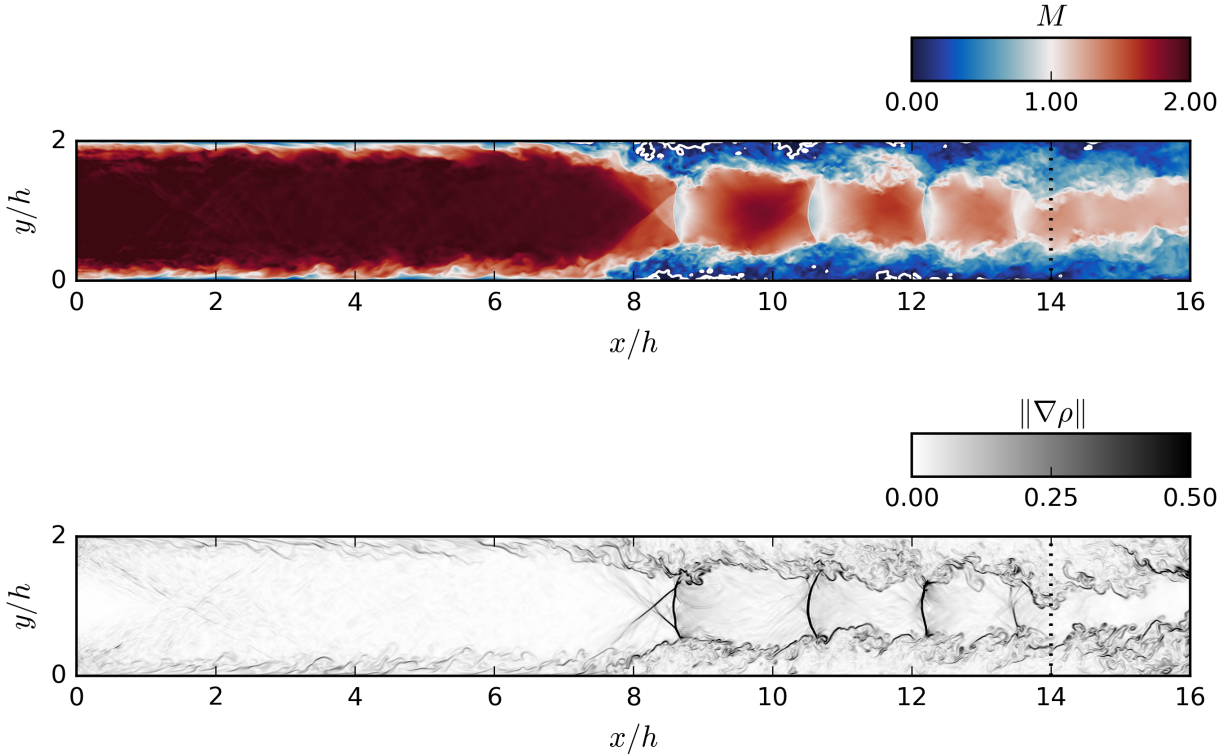
Fig. 2 **Instantaneous flow contours of Mach number (above) and density gradient (below) showing the typical shock train arrangement. The edge of the sponge zone is indicated by the dashed black line. For the Mach number plot, isolines of $M = 0$ (separation) are drawn in white.**

static pressure. For both cases the results represent the converged state of the shock train and the sampling time for statistics is $64h/u_1$ (roughly three full convective cycles if we assume an average convection velocity of $\bar{u} \sim 0.75u_1$).

The shock locations can be seen clearly in fig 3a as the sharp peaks in pressure. The wall pressure has a much more gradual rise due to the subsonic turbulent flow in the boundary layer region. It is clear from these results that the coarser grid resolution leads to a downstream shift in the shock positions (measured at $0.50h$) although the overall structure of the shock train is maintained. In fig 4 we plot the centerline pressure again but with the profiles adjusted to match the location of the first shock (x_3). Here, the two plots are extremely well-matched through the entire shock train which strongly suggests that the Baseline grid is able to reliably predict the shock train structure, including the strength and spacing of the shock waves.

In order to assess the sensitivity of the dynamic shock train behavior, both cases were subjected to a back pressure step change. Initially, a back pressure of $2.75p_1$ is applied and the shock train settles to an equilibrium position. At time t_0 the back pressure is changed instantaneously to $2.5p_1$ which causes the shock train to adjust its position in the domain before a new equilibrium is found. The Baseline grid case is sampled at a frequency of $0.08h/u_1$ whereas the Fine grid is sampled at a much larger interval of $4h/u_1$. The time evolution of the leading shock location for both grid
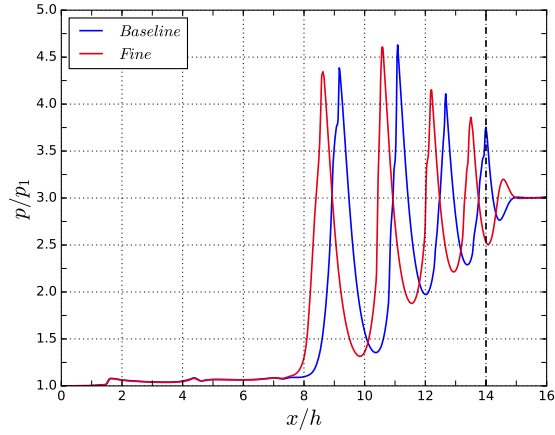
(a) Centerline pressure.
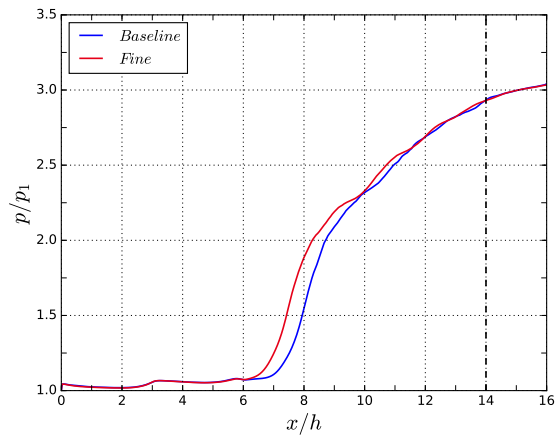
(b) Wall pressure.

Fig. 3   Comparison of pressure distributions for the different grid resolutions.
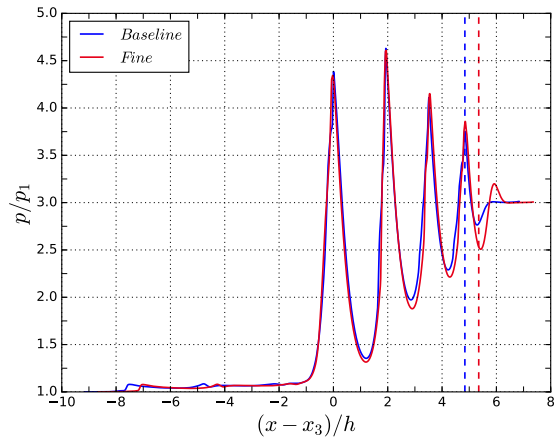

Fig. 4   Plots of centerline pressure, normalized by the leading shock position.

resolutions is given in fig 5. While the initial and final positions of the leading shock are different (Fine grid settles further upstream, as with fig 3) the trajectory and settling time (approximately $100h/u_1$) are consistent. Given that the

shock spacing is well conserved during the step response (see section III) we are confident that the dynamic behavior of the shock train is well captured by the coarser grid resolution.
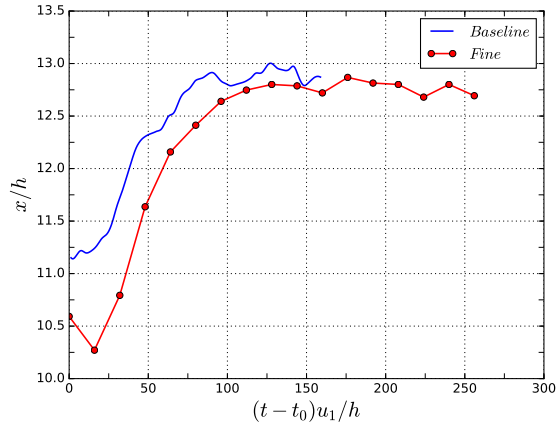
Fig. 5   Time evolution of the leading shock position after a back pressure step change at time t_0.

The Fine grid resolution is used for the cases in section III.A, while the Baseline grid is used for the cases in section III.B and IV where much longer run times are required.

C. Scheme Sensitivity Study

In this section we consider the sensitivity of the shock train system to the dissipation level of the TENO scheme. Such is the nature of shock capturing schemes, there is always a trade off between stability (high dissipation) and numerical accuracy (low dissipation). As discussed, the controlling parameter for dissipation in the TENO scheme is the cut-off parameter (C_T) and the benchmark value for these kinds of shock/turbulence problems (i.e. the C_T value which generally produces acceptably accurate and stable simulations) is 10^{-6}. However some of the moving shock train cases in section IV were found to be numerically unstable, leading to a value of $C_T = 10^{-5}$ being chosen. It was therefore important to test for the effect of different C_T values and these results are given in figure 6a where we compare distributions of centerline pressure and skin friction coefficient as well as density-weighted RMS profiles at $x = 6.2h$. Both cases use the Baseline grid resolution and a fixed back pressure of $3.0p_1$.

The pressure distribution (fig 6a) shows that the cut-off parameter has very little effect on either the intensity or location of the shock waves. Although the skin friction coefficient is typically a very sensitive parameter, the results in fig 6b indicate that the two distributions are very well matched through the upstream boundary layer and separation region. After the reattachment point (around $x = 10h$) there is a slight divergence suggesting that the cut-off parameter does have some effect on the dissipation in the latter half of the shock train. The turbulence intensity profiles (measured at the end of the development region) again show very good agreement between the two cases. One surprising result occurs at the peak of the $\xi\sqrt{\overline{u'u'}}/u_\tau$ curves where the high dissipation case ($C_T = 10^{-5}$) predicts a higher peak of turbulence intensity. This effect can be attributed to the fact that the skin friction is underestimated and hence the

11
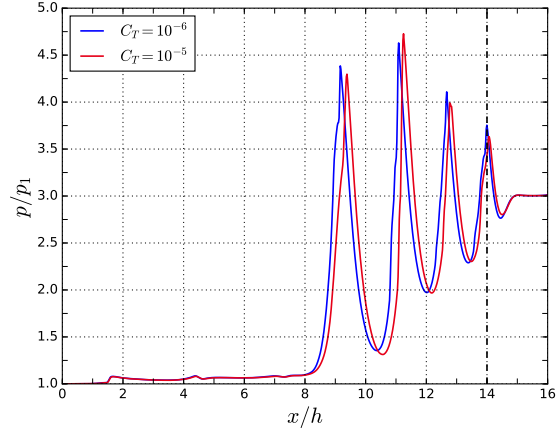
(a) **Distribution of centerline pressure.**
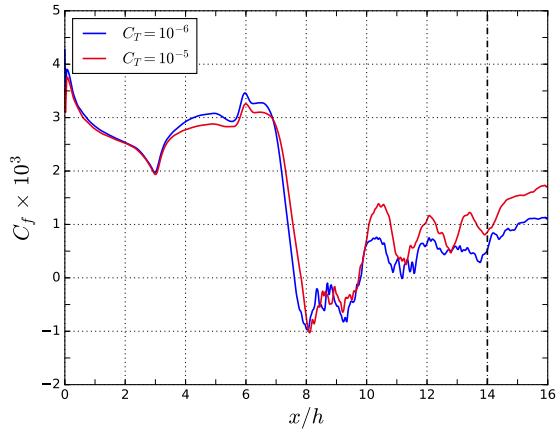
(b) **Distribution of skin friction coefficient.**
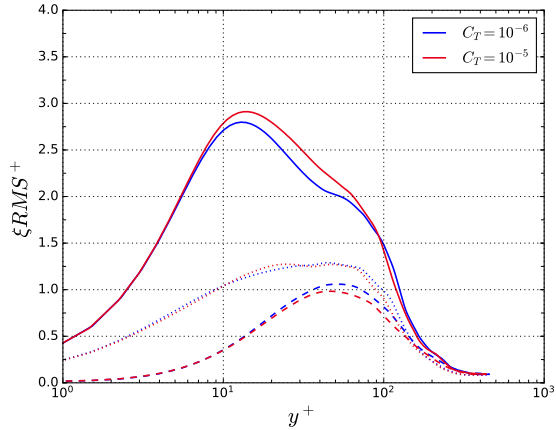
(c) **Turbulence intensity profiles at** $x = 6.2h$. **Solid lines =**
$\xi\sqrt{\overline{u'u'}}/u_\tau$; **Dashed =** $\xi\sqrt{\overline{v'v'}}/u_\tau$; **Dotted =** $\xi\sqrt{\overline{w'w'}}/u_\tau$.
$\xi = \sqrt{\rho/\rho_w}$ **is a density weight parameter.**

Fig. 6   Sensitivity of TENO cut-off parameter.

$1/u_\tau$ scaling of the velocity values is overestimated. When the scaling factor is removed and the raw fluctuations are considered, the peaks are within 2%.

Overall, the sensitivity to the cut-off parameter appears to be less than that of the grid resolution and therefore there does not seem to be an appreciable additional penalty in increasing the dissipation for the unsteady back pressure cases.

III. Fixed Back Pressure and Step Response Cases

A. Fixed Back Pressure Effects

Due to the use of time-dependent back pressures in the following sections, it was first necessary to understand the specific effects of a fixed back pressure. The cases in this study are outlined in table 3. The back pressures are selected such that the pressure ratios (p_b/p_1) over the channel are 3.0, 2.75 and 2.5. The Baseline case discussed here is identical to the Fine grid case previously shown in the grid refinement study. Given that shock trains are formed in response to high back pressures it is expected that, all else being equal, a lower back pressure will result in a shorter shock train with fewer shock waves (Klomparens et al. [9] for example, found a linear relationship between the back pressure and the location of the shock train leading edge).

Table 3   Summary of cases for the back pressure study.

Case	Grid	p_b	p_b/p_1
BP300	Fine	0.536	3.0
BP275	Fine	0.446	2.75
BP250	Fine	0.357	2.5

The data from each case has been averaged over a period of $64h/u_1$ and the centerline pressure results are shown in figure 7. As expected, the size of the back pressure is positively correlated with the length of the shock train and therefore the number of shocks. In figure 8 we plot the effect of back pressure on shock location as well as shock train leading edge position (x_2, defined as where the wall pressure rises 5% above the natural pressure rise in the channel).

Within the range of the back pressures studied, there appears to be a linear relationship between back pressure and shock location (indicated by the dashed lines). This is consistent with Klomparens et al. [9] as well as Carroll & Dutton [5] who found a similar linear dependence. The x_2 line intersects the domain outlet at approximately $p_b/p_1 = 1.9$ and the edge of the sponge zone at $p_b/p_1 = 2.1$, suggesting that the minimum back pressure needed to cause an incipient shock train to form in this channel lies within this range.

As with the grid study, the normalized pressure distributions (shown on fig 9) align closely, demonstrating that that the relative positions of the shock waves as well as the flow structure between them are largely independent of the size of the back pressure. Similar findings have been presented in the past [5, 13], although only for the wall pressure
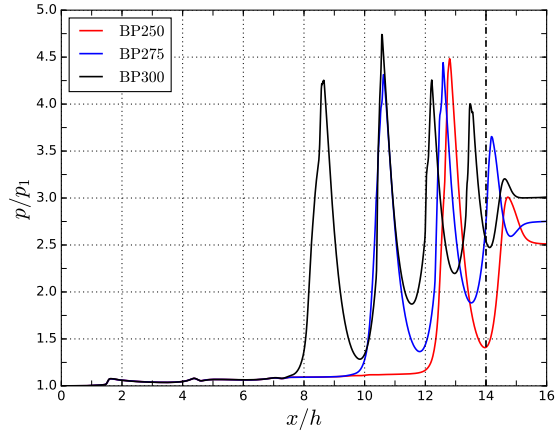
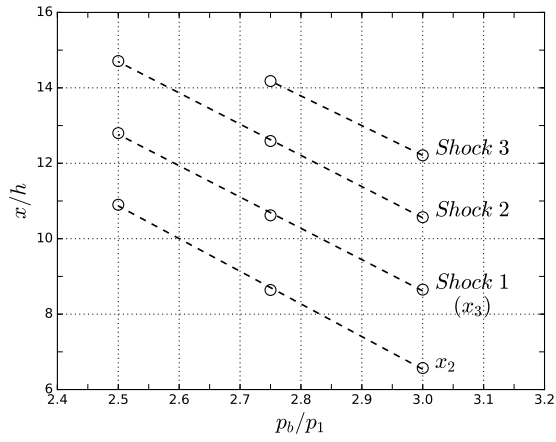**Fig. 7   Effect of back pressure size on centerline pressure distribution.**

Fig. 8   Effect of back pressure on shock location.
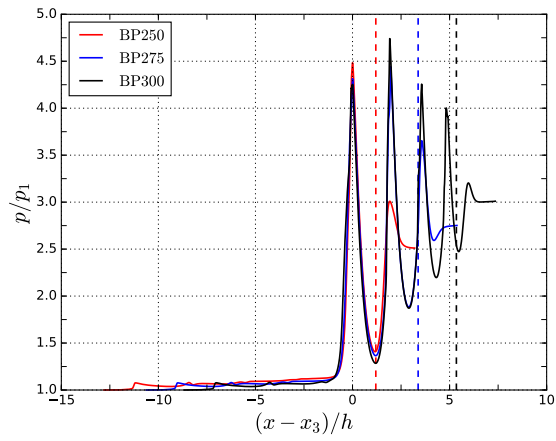
distribution.

Fig. 9   Normalized centerline pressure distribution at different back pressures.

B. Step Forcing

The step forcing is conducted on a steady state shock train where the back pressure is instantaneously stepped up or down at time t_0. The four cases discussed here have differing initial back pressures and step sizes as outlined in table 4. The results for all four cases are given in fig 10. As expected, step increases (fig 10b and 10d) cause the shock waves to move upstream, increasing the length of the shock train, with the reverse effect for step decreases (fig 10a and 10c). In fig 10a there is a clear lag in the shock response as the back pressure signal is transmitted upstream at approximately $0.17u_1$.

Table 4   List of step change cases.

Test case	Grid	Initial p_b/p_1	Final p_b/p_1	$\|\Delta p/p_1\|$
C25-275	Baseline	2.50	2.75	0.25
C275-25	Baseline	2.75	2.50	0.25
C25-30	Baseline	2.50	3.00	0.5
C30-25	Baseline	3.00	2.50	0.5

(a) $C30-25$.

(b) $C25-30$.

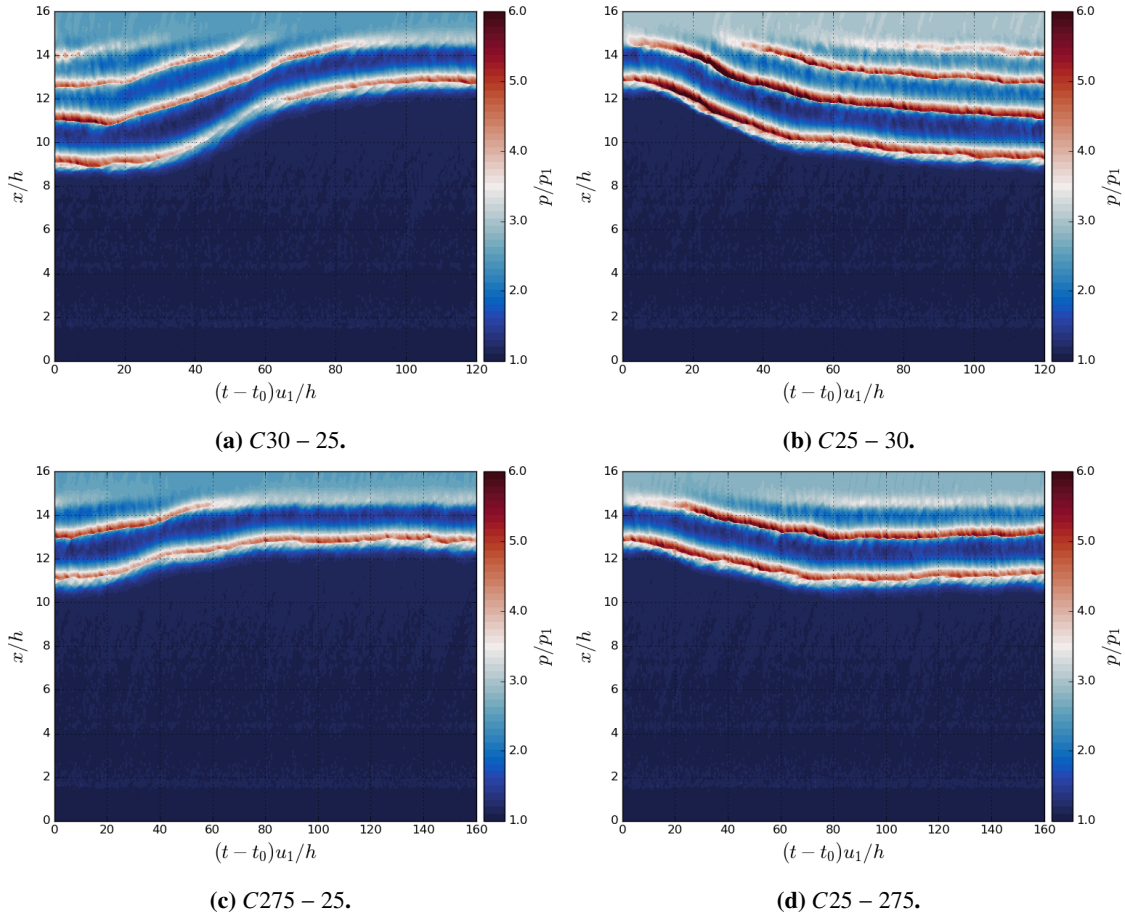**(c)** $C275-25$.

(d) $C25-275$.

Fig. 10   Step response simulation results.

The trajectories of the leading shocks are plotted in fig 11 in order to provide a clear comparison between the responses. In fig. 11a we plot the coordinates showing that the shock speed decreases as the shock approaches the new equilibrium position. In fig. 11b we plot the same coordinates but normalized by the lag time, t_{lag}, between the back pressure change and the shock response. Additionally, we take the absolute value of the corrected coordinate, $\|x - x_1\|$, in order to correct for the direction of the step change. The results of the corrected shock trajectories show that there is a high degree of symmetry between step up/step down when the step size is the same, as seen by the collapse of the blue and black curves.
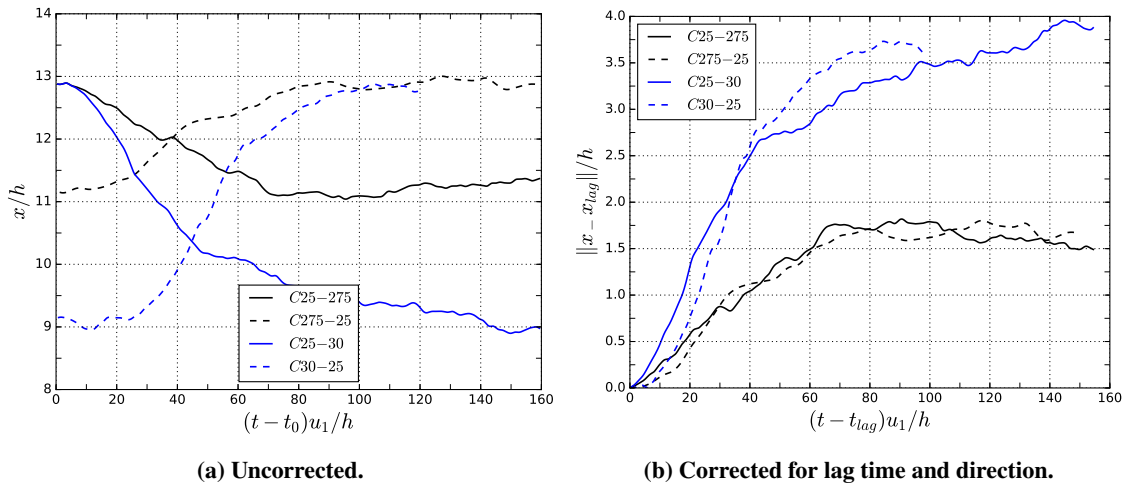

(a) Uncorrected.

(b) Corrected for lag time and direction.

Fig. 11   Corrected and uncorrected leading shock trajectories in $x-t$ space.

Within the time period $(t - t_{lag})u_1/h < 40$ the C25-30 case moves a distance of approximately $2.5h$ compared with $1.1h$ for the C25-275 case. This is a factor of 2.3 difference whereas the pressure change differs by a factor of 2.0, suggesting an approximately linear relation of the response rate to the imposed step amplitude. Having only two cases to compare limits any further interpretation of the relationship that can be inferred between these two variables but it is clear that a higher back pressure change has a corresponding effect on the initial response of the shock train. The settling time (the time after t_{lag} taken to reach a new equilibrium position) for the lower step size cases are very similar at around $80h/u_1$ suggesting a good degree of symmetry. The settling time of the C30-25 case is also around $80h/u_1$ but the C25-30 takes considerably longer (around $120h/u_1$) to reach the average position for $p_b = 2.5p_1$ back pressure.

In fig 12 we compare the time-averaged centerline pressure distribution of C30-35 and C25-30 to that of a shock train at fixed back pressure $(3.0p_1)$ over the first two shock waves. The data is collected between $30h/u_1$ and $80h/u_1$ when the shock trains are moving and the plots have been shifted to account for the time-dependent values of x_3 (the leading shock) and x_4 (the second shock). Comparing the pressure through both shocks, it is clear that when the shock train is moving upstream (C25-30) the peak shock pressure increases (and vice-versa) relative to the static shock train case. This is consistent with fig 10 where the shock lines darken/lighten in color as the shock moves upstream/downstream.

16
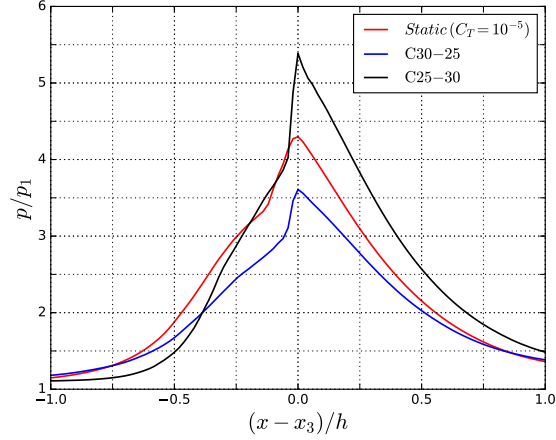
(a) Leading shock.
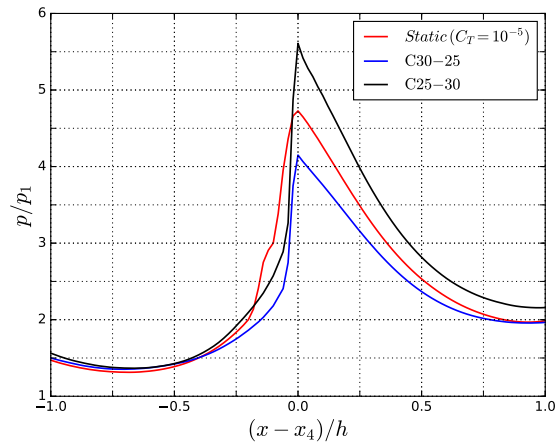
(b) Second shock.

Fig. 12   Normalized centerline pressure distributions for moving and static shock trains.

IV. Sinusoidal Back Pressure Effects

A. Time History Analysis

Due to the flow conditions experienced by a typical shock train within an air-breathing engine, it is important to understand the response of shock trains to harmonic back pressure variations. For example, the operation cycle of a combustion chamber can induce periodic loads which may reach the shock train within the isolator section. In this section we will study the response of a shock train to three separate back pressure forcing frequencies. Here, the time varying back pressure takes the form

$$p_b(t)/p_1 = \begin{cases} 3.0 & t < t_0 \\ 3.0 + \sin\left(\frac{2\pi(t-t_0)}{T_0}\right) & t > t_0, \end{cases} \tag{10}$$

where T_0 is the period of oscillation. The oscillations begin at time t_0 when the shock train is assumed to be at a steady

17

state. This results in an average back pressure of 3.0 and maxima and minima of 4.0 and 2.0. The chosen oscillation periods and the corresponding frequencies are listed in table 5. The conversion into kHz is done using an assumed reference freestream velocity of $680 m/s$ and a channel length, l_x, of $70mm$ *. Since the flow-through time period is approximately $21h/u_1$ the three cases allow for respectively 5.3, 1.3 and 0.33 oscillation periods per convective cycle. Oscillation data is captured over a long enough time frame that the shock train responses become cyclic.

Table 5   List of back pressure forcing frequencies.

Case	Grid	T_0 (h/u_1)	f (u_1/h)	f (kHz)
T-04	Baseline	4	0.25	40
T-16	Baseline	16	0.0625	10
T-64	Baseline	64	0.015625	2.5

In fig 13 contour plots of the time history of centerline pressure are shown for each applied frequency (a fixed pressure case is included to show the level of natural unsteadiness due to upstream turbulence). The back pressure oscillations apply uniformly across the sponge zone ($x/h > 14$) when they then travel upstream through the shock train. It is immediately clear that the different forcing frequencies induce very different shock train responses. The highest frequency case (T-04) only noticeably affects the two downstream shock waves, causing them to oscillate slightly. Any disturbances upstream of this are quickly dissipated. As seen in section III the natural settling time of the shock train is of the order $100h/u_1$ and therefore the forcing period ($4h/u_1$)is too low to cause any significant shock train response.

The intermediate forcing frequency in T-16 causes much larger oscillations in the shock wave positions. All but one of the shock waves oscillate in the streamwise direction at the applied forcing frequency. The leading shock oscillates initially at roughly half the applied frequency before converging to a new equilibrium position. The forcing pushes the downstream shocks further upstream and, with other shock spacings preserved along the shock train, the leading shock ends up $\sim 1.5h$ upstream of its original position.

By decreasing the frequency further still (T-64), the shock wave oscillations become even larger. Each forcing cycle causes the production and subsequent destruction of three separate shock waves. During the high pressure ($p_b/p_1 > 3.0$) periods three individual shocks form and begin to travel upstream until they are met with retreating shocks from the previous cycle. At this point there is a complex but repeatable merging process between the retreating and advancing shocks.

The combined effect of the back pressure lag and the shock train merging process is for the oscillation pattern of the leading shock to have a saw-tooth wave form, rather than a smooth sinusoidal shape. As with the T-16 case, the average position becomes significantly offset from the initial state. This phenomenon appears to be indirectly caused by the lag time between forcing and response. When the back pressure is high, the disturbances travel upstream and force the

---

*These values are based on assuming a reference pressure of 10 kPa and reference temperature of 273 K.

(a) Fixed back pressure.

(b) $T_0 = 4h/u_1$.

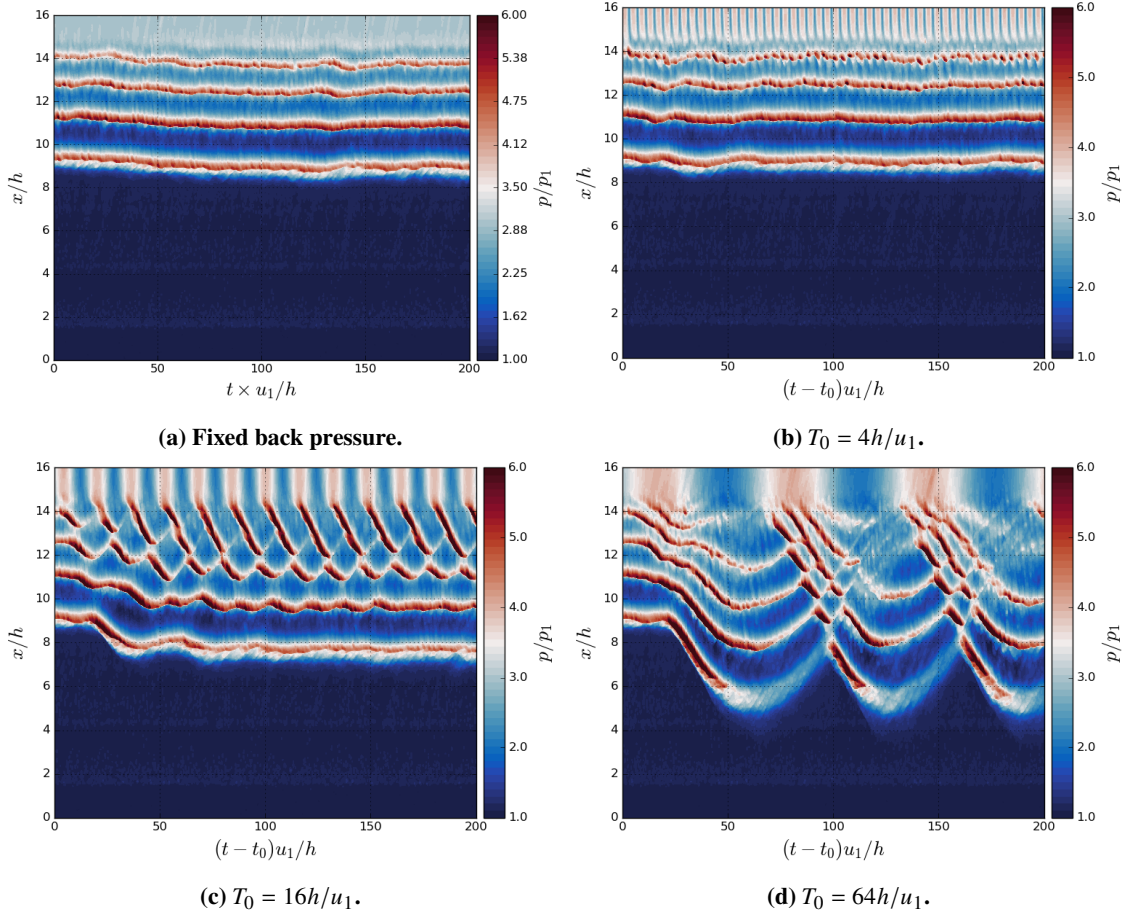**(c)** $T_0 = 16h/u_1$.

(d) $T_0 = 64h/u_1$.

Fig. 13   Shock train response to harmonic back pressure forcing at different frequencies.

shocks to also move upstream. As a result of traveling in the same direction, the shocks spend more time responding to higher pressure ($> 3.0p_1$) parts of the cycle than low pressure, and therefore there is an upstream bias in the system. As seen in fig 14, all of these results are independent of the initial phase of the forcing function, albeit after two complete oscillation cycles.
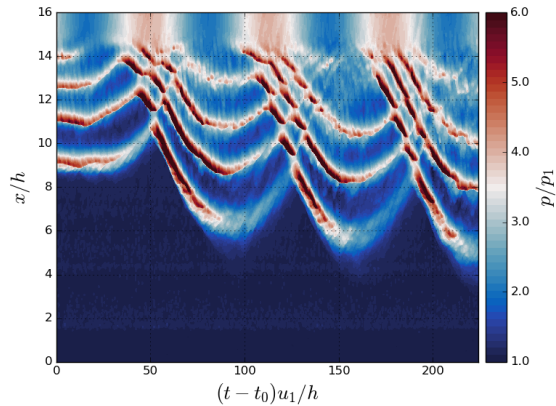

Fig. 14   T-64 shock train response with $180°$ phase difference in forcing function.

The large oscillation amplitudes are enough to move the leading shock temporarily into the boundary layer development region ($x/h < 6$) so the T-64 case was run again on a longer domain (up to $24h$) in order to avoid this, with the result shown in fig 15. The longer domain affects the boundary layer thickness that is encountered by the shock train and thus we see that there is a higher number of shocks that appear. Additionally, the strength (pressure peak) of the leading shock does not drop as much before reaching the maximum oscillation amplitude and reduces more gradually as the shock moves downstream. Despite this, we observe a very similar upstream offset of the leading shock (around $3h$) and the same interference pattern between advancing and receding shock waves.
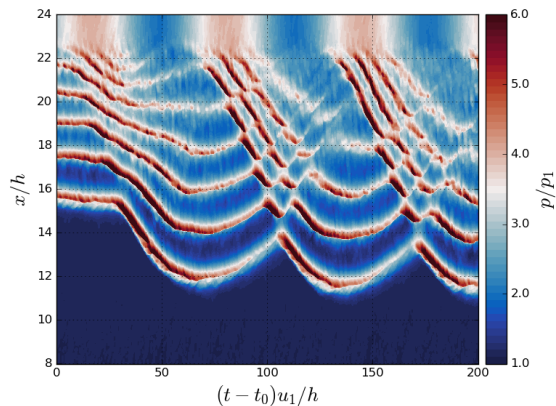

Fig. 15   Longer domain version of the T-64 case.

A visualization of the shock interference process of the T-64 case is given in fig 16 (in particular, the interference between the second and third shocks just after $100h/u_1$ in figure 13d). Here we show Mach number contours aligned with centerline pressure plots at three separate time instances. At the first time instance (fig 16a) there is a weaker upstream shock moving towards a stronger downstream shock. The relative strengths of these shocks is consistent with the data from the moving shocks in fig 12. In fig 16b the shocks have moved closer together and their peak pressure is now matched. At this instant the shocks reach their minimum separation distance which is around half of the natural spacing of the static shock train. After this occurs (fig 16c), the shocks then move apart with the upstream shock now being the stronger of the two. The interference process may be considered either as two moving shock waves either passing through each other or reflecting off each other. In the former interpretation, a shock wave which forms at the outlet can pass through the entire shock train to eventually become the leading shock, before eventually retreating back to the outlet.

The range of frequencies considered here are significantly higher than the majority of those that have been previously published. Even when adjusting for the domain size, the applied back pressure forcing in both [13] and [12] occurs at frequencies at least one order of magnitude below that of the current work. At such frequencies the lag effect between the head and tail of the shock train becomes negligible and each of the shock waves can be assumed to be in an equilibrium position with respect to the time-varying back pressure. Hence, these cases did not observe any of the
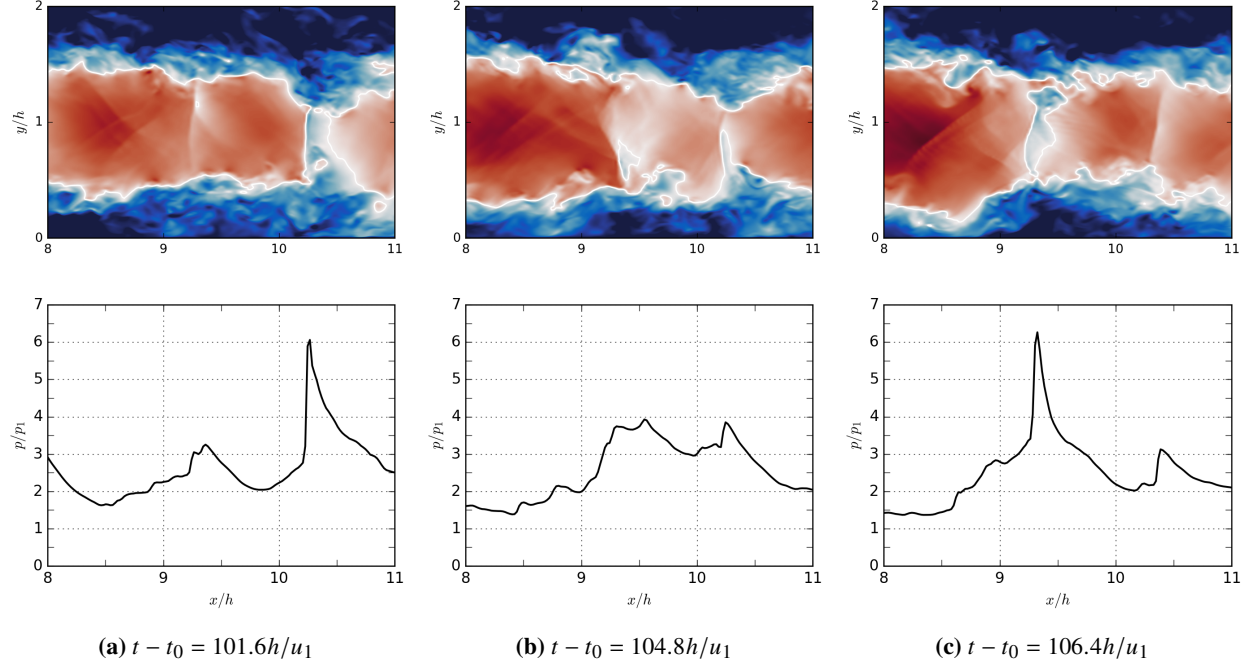
20

(a) $t - t_0 = 101.6h/u_1$ **(b)** $t - t_0 = 104.8h/u_1$ **(c)** $t - t_0 = 106.4h/u_1$

Fig. 16 Instantaneous flow contours (Mach number) and corresponding centerline pressure distributions showing the shock interference process.

frequency-dependent behavior (shock merging, dissipation of disturbances) that are seen here. Back pressure forcing at a similar frequency range to the current work has been considered in [15] where some of the same frequency-dependent behavior was observed, although there was no detailed account of the shock train time-history.

B. Spectral Analysis

In this section we consider the power spectra of wall pressure fluctuations in order to gain a better understanding of the shock train dynamic behavior. Here we are concerned with a non-dimensional frequency, namely the Strouhal number, where the reference length is taken as the channel half-height, h, given by

$$St_h = \frac{fh}{u_1}. \tag{11}$$

All three frequency cases are considered here[†] as well as a case with a fixed back pressure ($p_b = 3.0p_1$). The cases were run over a time period of $360h/u_1$ ($200h/u_1$ for the fixed back pressure case) and sampled at an interval of $0.08h/u_1$. Data is captured over one entire wall and the spectra are computed at each x and z position using Welch's method [29] with a Blackman window applied to each segment in order to reduce any spectral leakage effects. The spectra at each streamwise position is then span-averaged. In fig 17 we show contours of power spectral density (PSD) in $St_h - x$ space for all four cases. Data for each case has been taken from one entire wall and three overlapping segments

---

[†]For the T-64 case the longer ($L_x = 24h$) domain is considered, to avoid interference with the boundary layer development region.

are used with Welch's method. A non-weighted PSD was preferred in this case so that all the key features can be seen using the same color scale.
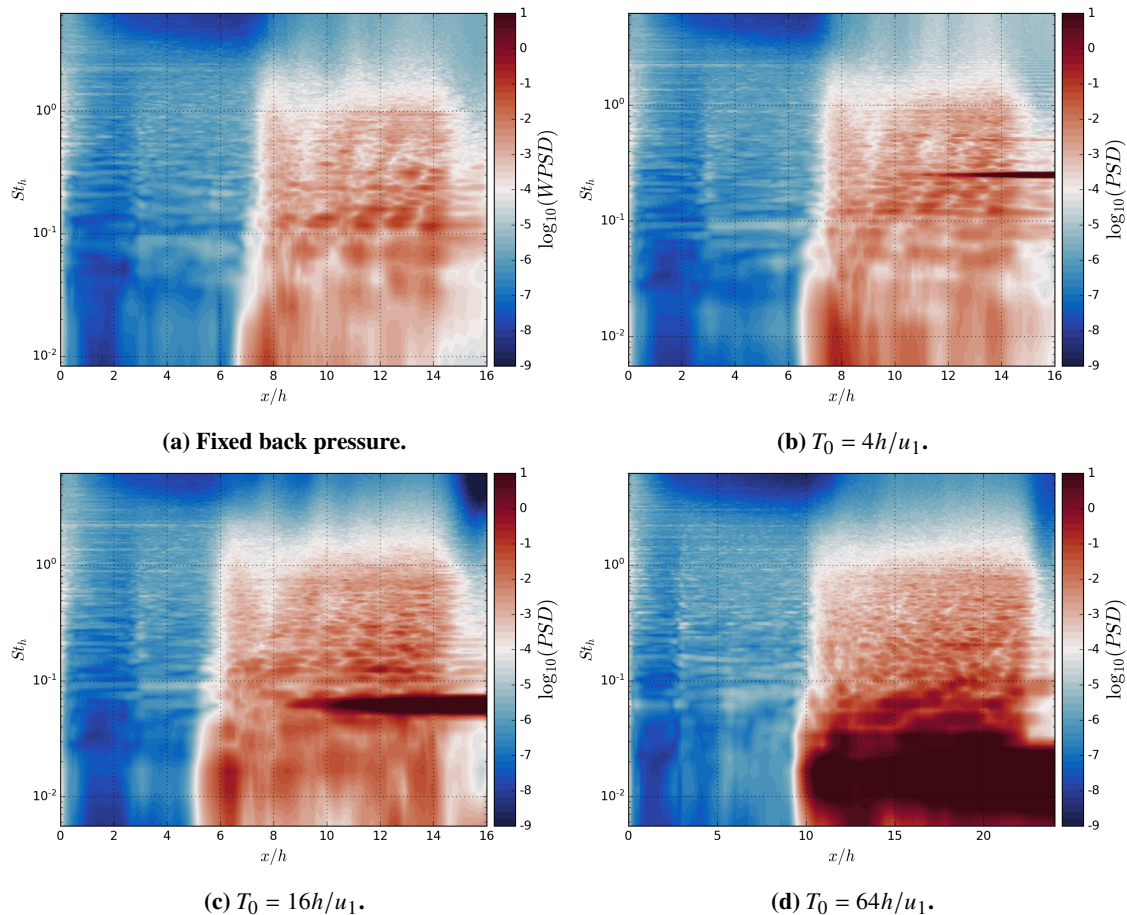

(a) Fixed back pressure.

(b) $T_0 = 4h/u_1$.

(c) $T_0 = 16h/u_1$.

(d) $T_0 = 64h/u_1$.

Fig. 17   Contours of power spectral density showing the spatial and frequency distribution of fluctuation intensity.

The shock train can be seen to be responsible for a broadband increase in pressure fluctuations. This is directly caused by the increase in turbulent mixing which occurs within the subsonic region. One feature that can be seen in figs 17 (a)-(c) is the region of low frequency oscillation that occurs at the leading edge of the shock train at around $x/h = 6-8$ and at a Strouhal number of approximately $St_h = 10^{-2}$. Interestingly, this is similar to the low frequency movement that is commonly observed at the shock foot location in incident-reflected SBLI problems. For example, [16] observed a peak in low frequency oscillations at the leading edge of the separation bubble, with the peak intensity at $St_L = fL_{sep}/u_1 \sim 0.03$. Given a value of $L_{sep} \sim 1.9h$ in the current work (as measured by the region of negative C_f) we arrive at $St_L \sim 0.02$ and hence the peak Strouhal numbers are of comparative size (it should be noted that this region of high amplitude occurs over a range of frequencies). This is consistent with [19], which suggested that the same leading shock motion may occur in shock train problems as with oblique and normal SBLIs.

For the sinusoidal back pressure cases shown in fig 17 (b)-(d), the applied forcing frequencies correspond to Strouhal

22

numbers of 0.25, 0.0625 and 0.0156 for the T-04, T-16 and T-64 cases respectively. The effect of the back pressure forcing is immediately obvious in each case due to the high-intensity line stretching from the outflow. It has been observed that upstream-propagating disturbances in shock interaction problems travel via the subsonic region near the wall [30]. It therefore seems plausible that this is the method of propagation of the disturbances through the shock train. For the T-04 and T-16 cases, the back pressure forcing appears to have limited influence on the flow as shown by the decay in the intensity of the fluctuations as they are carried further upstream. The disturbances have entirely disappeared by $x = 10h$ and $x = 8h$ for the T-04 and T-16 cases respectively. Additionally, in both these cases, the low frequency peak at the leading shock can be seen suggesting that this phenomenon remains unaffected (other than the offset in position in T-16). It may be useful to consider the shock train as a low-pass filter, whereby high frequency disturbances from the outflow are dissipated before reaching the leading edge of the shock train. A similar filtering effect was observed by [2] with high frequency inlet disturbances.

The low frequency forcing in T-64 has a much larger impact on the PSD field. Not only do the disturbances dominate the frequencies $St_h = 0.05$ and below, but the influence extends all the way to the leading shock. The oscillation of the leading shock becomes locked-in to the applied frequency, as observed in fig 13d with the sawtooth-like waveform in $x - t$ space. It is clear that the period of oscillation in this case is large enough to prevent the disturbances becoming dissipated as they pass upstream. With respect to the natural low-frequency oscillation seen under the leading shock foot, we see that this can be influenced by downstream disturbances in the right frequency band. The response under the leading shock foot is enhanced by several orders of magnitude in the PSD representation, showing that downstream unsteadiness can be a source of the low-frequency unsteadiness under a shock foot. The amplitude is sufficiently high in the present low-frequency case that the downstream response dominates over the local response of the separating turbulent boundary layer.

By observing the time history and frequency data we can isolate the main determinants of the shock train response to sinusoidal forcing. These are: (1) the forcing-response time lag of the disturbances; (2) the ratio of the forcing period to the natural settling time of the shock train (the latter being of the order $100h/u_1$ as seen in section III, albeit with lower forcing amplitudes); (3) the low pass filtering effect which dissipates the higher frequency disturbances; and finally, (4) the natural geometric shock spacing of the shock train. Additionally, the amplitude of the back pressure forcing (which is not assessed here) is another key factor in determining the shock train response [12, 15]. As discussed, a combination of (1) and (4) are responsible for the upstream offset of the leading shock. The shock interference behavior observed in the previous section requires large shock oscillation amplitudes and a finite forcing lag and therefore is determined by both features (1) and (2).

Features (1) and (2) are only relevant when the Strouhal number of the forcing is sufficiently high (i.e. when the forcing period is too short for the shock train to settle on an equilibrium). Feature (3) is also dependent on the frequency of the forcing but may also depend on the Reynolds number of the system due to the interaction of the disturbances with

23

the turbulent flow near the wall. Further investigation would be needed to determine whether geometric similarity is sufficient to reproduce the filtering of high frequency disturbances.

V. Conclusions

In the current work we have presented the results of numerical simulations that have been performed on shock trains in the development region of a channel with turbulent boundary layers at the inflow. A validation study was performed on a shock train with upstream conditions $M = 2$, $Re_\theta = 500$ in order to understand the sensitivity of the results to the level of grid refinement and the dissipation of the numerical scheme. It was found that the shock train equilibrium position is sensitive to both factors but that the pressure distribution through the shock train (including the shock strength and spacing) is not. In the first part of the study the expected linear correlation between the back pressure and the length of the shock train was confirmed. It was also observed that the shock strength, shock spacing and post-shock expansion are all independent of the back pressure. Tests were also made to determine how the shock train responds to sudden increases or decreases in back pressure. The results show that the back pressure changes induce strong responses on the shock train, causing each of the shock waves to move at an approximately constant speed (upstream movement for positive changes and vice-versa). Additionally, upstream and downstream shock movements were found to be associated with, respectively, increased and reduced centerline shock pressures. After an initial period of shock movement, the shock speed gradually reduces before converging on the new equilibrium position. The main factor affecting the initial response was found to be the size of the pressure jump, where a larger step change induces a faster response. Additionally the step up/down response appears to be symmetrical for the same absolute step change.

The main interest of this work is on time-dependent back pressure and in particular the shock train response to sinusoidal forcing at three separate frequencies was studied. At the highest frequency ($St_h = 0.25$) the back pressure disturbances are dissipated within a short distance of the outflow and the overall impact on the shock train is low. For the medium frequency ($St_h = 0.0625$) the oscillations of the downstream shocks are larger and the position of the leading shock is shifted significantly upstream. The lowest forcing frequency ($St_h = 0.0156$) causes very large oscillations for all of the shocks and the forcing response time-lag produces a complex interference process between advancing and receding shocks. An analysis of the wall pressure spectra reveals a region of low frequency motion under the leading shock similar to that of canonical incident-reflected SBLI problems. At the lowest frequency it was shown how the back-pressure forcing became coupled to the low-frequency oscillation under the leading shock foot. The spectral analysis also provides further demonstration of the dissipation of high frequency back pressure disturbances as well as illuminating the mechanism by which downstream disturbances can significantly enhance the low frequency response under the foot of a shock wave.

Acknowledgments

References

[1] Matsuo, K., Miyazato, Y., and Kim, H. D., "Shock train and pseudo-shock phenomena in internal gas flows," *Progress in Aerospace Sciences*, Vol. 35, No. 1, 1999, pp. 33–100. https://doi.org/10.1016/S0376-0421(98)00011-6.

[2] Fiévet, R., Koo, H., Raman, V., and Auslender, A. H., "Numerical investigation of shock-train response to inflow boundary-layer variations," *AIAA Journal*, Vol. 55, No. 9, 2017, pp. 2888–2901. https://doi.org/10.2514/1.J055333.

[3] Weiss, A., Grzona, A., and Olivier, H., "Behavior of shock trains in a diverging duct," *Experiments in Fluids*, Vol. 49, No. 2, 2010, pp. 355–365. https://doi.org/10.1007/s00348-009-0764-9.

[4] Morgan, B., Duraisamy, K., and Lele, S. K., "Large-eddy simulations of a normal shock train in a constant-area isolator," *AIAA Journal*, Vol. 52, No. 3, 2014, pp. 539–558. https://doi.org/10.2514/1.J052348.

[5] Carroll, B. F., and Dutton, J. C., "Characteristics of multiple shock wave/turbulent boundary-layer interactions in rectangular ducts," *Journal of Propulsion and Power*, Vol. 6, No. 2, 1990, pp. 186–193. https://doi.org/10.2514/3.23243.

[6] Hunt, R. L., and Gamba, M., "Shock train unsteadiness characteristics, oblique-to-normal transition, and three-dimensional leading shock structure," *AIAA Journal*, Vol. 56, No. 4, 2018, pp. 1569–1587. https://doi.org/10.2514/1.J056344.

[7] Cox-Stouffer, S., and Hagenmaier, M., "The effect of aspect ratio on isolator performance," *39th AIAA Aerospace Sciences Meeting and Exhibit*, 2001, p. 519. https://doi.org/10.2514/6.2001-519.

[8] Carroll, B., and Dutton, J. C., "Characteristics of multiple shock wave/turbulent boundary layer interactions in rectangular ducts," *1st National Fluid Dynamics Conference*, 1988, pp. 1340–1347. https://doi.org/10.2514/6.1988-3803.

[9] Klomparens, R., Driscoll, J., and Gamba, M., "Unsteadiness characteristics and pressure distribution of an oblique shock train," *53rd AIAA Aerospace Sciences Meeting*, 2015. https://doi.org/10.2514/6.2015-1519.

[10] Billig, F. S., "Research on supersonic combustion," *Journal of Propulsion and Power*, Vol. 9, No. 4, 1993, pp. 499–514. https://doi.org/10.2514/3.23652.

[11] Roussel, C., "Modelisation et simulation de l'interaction onde de choc/couche limite turbulente en écoulement interne avec effets de coins," Ph.D. thesis, Paris, ENSAM, 2016.

[12] Gnani, F., Zare-Behtash, H., White, C., and Kontis, K., "Effect of back-pressure forcing on shock train structures in rectangular channels," *Acta Astronautica*, Vol. 145, 2018, pp. 471–481. https://doi.org/10.1016/j.actaastro.2018.02.010.

[13] Klomparens, R., Driscoll, J. F., and Gamba, M., "Response of a shock train to downstream back pressure forcing," *54th AIAA Aerospace Sciences Meeting*, 2016. https://doi.org/10.2514/6.2016-0078.

[14] Edelman, L. M., and Gamba, M., "Rigid Body Response of a Mach 2 Shock Train to Downstream Forcing," *2018 Fluid Dynamics Conference*, 2018. https://doi.org/10.2514/6.2018-3542.

[15] Jiao, X., Chang, J., Wang, Z., and Yu, D., "Periodic forcing of a shock train in a scramjet inlet-isolator at overspeed condition," *Acta Astronautica*, Vol. 143, 2018, pp. 244–254. https://doi.org/10.1016/j.actaastro.2017.12.005.

[16] Touber, E., and Sandham, N. D., "Large-eddy simulation of low-frequency unsteadiness in a turbulent shock-induced separation bubble," *Theoretical and Computational Fluid Dynamics*, Vol. 23, No. 2, 2009, pp. 79–107. https://doi.org/10.1007/s00162-009-0103-z.

[17] Dupont, P., Haddad, C., and Debieve, J., "Space and time organization in a shock-induced separated boundary layer," *Journal of Fluid Mechanics*, Vol. 559, 2006, pp. 255–277. https://doi.org/10.1017/S0022112006000267.

[18] Touber, E., and Sandham, N. D., "Low-order stochastic modelling of low-frequency motions in reflected shock-wave/boundary-layer interactions," *Journal of Fluid Mechanics*, Vol. 671, 2011, pp. 417–465. https://doi.org/10.1017/S0022112010005811.

[19] Xiong, B., Fan, X. Q., Wang, Y., Zhou, L., and Tao, Y., "Back-pressure effects on unsteadiness of separation shock in a rectangular duct at Mach 3," *Acta Astronautica*, Vol. 141, 2017, pp. 248–254. https://doi.org/10.1016/j.actaastro.2017.09.032.

[20] Jacobs, C. T., Jammy, S. P., and Sandham, N. D., "OpenSBLI: A framework for the automated derivation and parallel execution of finite difference solvers on a range of computer architectures," *Journal of Computational Science*, Vol. 18, 2017, pp. 12–23. https://doi.org/10.1016/j.jocs.2016.11.001.

[21] Lusher, D. J., Jammy, S. P., and Sandham, N. D., "Shock-wave/boundary-layer interactions in the automatic source-code generation framework OpenSBLI," *Computers & Fluids*, Vol. 173, 2018, pp. 17–21. https://doi.org/10.1016/j.compfluid.2018.03.081.

[22] Fu, L., Hu, X. Y., and Adams, N. A., "A family of high-order targeted ENO schemes for compressible-fluid simulations," *Journal of Computational Physics*, Vol. 305, 2016, pp. 333–359. https://doi.org/10.1016/j.jcp.2015.10.037.

[23] Lusher, D. J., and Sandham, N. D., "Assessment of Low-Dissipative Shock-Capturing Schemes for the Compressible Taylor–Green Vortex," *AIAA Journal*, Vol. 59, No. 2, 2021, pp. 533–545. https://doi.org/10.2514/1.J059672.

[24] Kennedy, C. A., and Carpenter, M. H., "Fourth-order 2N-storage Runge-Kutta schemes," Tech. rep., NASA Langley Research Center, 1994.

[25] Gillespie, A., "Direct Numerical Simulations of Shock Trains," Ph.D. thesis, University of Southampton, 2021. https://doi.org/10.5258/SOTON/D1770.

[26] Geerts, J. S., and Yu, K. H., "Systematic application of background-oriented schlieren for isolator shock train visualization," *AIAA Journal*, Vol. 55, No. 4, 2017, pp. 1105–1117. https://doi.org/10.2514/1.J054991.

[27] Kim, Y., Xie, Z.-T., and Castro, I. P., "A forward stepwise method of inflow generation for LES," *Proceeding of the 6th International Conference on Fluid Dynamics*, Vol. 1376, AIP, 2011, pp. 134–136. https://doi.org/10.1063/1.3651856.

[28] Kim, Y., "Wind turbine aerodynamics in freestream turbulence," Ph.D. thesis, University of Southampton, 2013.

[29] Barbe, K., Pintelon, R., and Schoukens, J., "Welch method revisited: nonparametric power spectrum estimation via circular overlap," *IEEE Transactions on Signal Processing*, Vol. 58, No. 2, 2009, pp. 553–565. https://doi.org/10.1109/TSP.2009.2031724.

[30] Sansica, A., Sandham, N. D., and Hu, Z., "Instability and low-frequency unsteadiness in a shock-induced laminar separation bubble," *Journal of Fluid Mechanics*, Vol. 798, 2016, pp. 5–26.